Geophysical Research Letters

RESEARCH LETTER
10.1029/2020GL089802

Key Points:
- We invert for multifault slip models of the 2019 Ridgecrest sequence with a novel subevent-guided slip inversion using 3-D Green's functions
- The *M*6.4 foreshock ruptured orthogonal faults and promoted the nucleation of the *M*7.1 mainshock at a complex junction point of three faults
- The slip of the *M*6.4 and *M*7.1 events are complementary on the main NW-SE fault plane, which is complex near surface but simple at depth

Supporting Information:
- Supporting Information S1
- Data Set S2
- Data Set S3

Correspondence to:
Z. Jia,
zjia@gps.caltech.edu

Citation:
Jia, Z., Wang, X., & Zhan, Z. (2020). Multifault models of the 2019 Ridgecrest sequence highlight complementary slip and fault junction instability. *Geophysical Research Letters*, *47*, e2020GL089802. https://doi.org/10.1029/2020GL089802

Received 14 JUL 2020
Accepted 21 AUG 2020
Accepted article online 30 AUG 2020

Multifault Models of the 2019 Ridgecrest Sequence Highlight Complementary Slip and Fault Junction Instability

Zhe Jia[1], Xin Wang[1], and Zhongwen Zhan[1]

[1]Seismological Laboratory, California Institute of Technology, Pasadena, CA, USA

Abstract The 2019 Ridgecrest M_w 6.4 and M_w 7.1 earthquakes ruptured a complex fault system, posing challenges in understanding their physical processes. Modeling of the ruptures relies on fault geometries at depth, which are usually assumed based on surface traces and aftershocks. Here we use seismic and geodetic data to jointly constrain the fault geometries and slip distributions. We first represent the first-order rupture processes with a series of subevents, then conduct slip inversions with subevent-guided fault geometries. We find that the foreshock sequentially ruptured the NW and SW striking faults starting from their junction. The mainshock initiated at a complex three-fault junction along the extension of the foreshock NW rupture, with major slip first occurring bilaterally near the hypocenter and then minor unilateral slip later to the southeast end. The slip distributions of the foreshock and mainshock are complementary to each other on the overlapping fault section.

Plain Language Summary Large earthquakes are often complicated, especially if they occur in relatively immature fault systems. Multiple subparallel or orthogonal surface fault traces may be involved in a single sequence. How the surface complexities extend to depth and impact earthquake rupture processes is critical for understanding earthquake physics and hazard but hard to assess. The 2019 July Ridgecrest sequence, which included a magnitude 6.4 foreshock, a magnitude 7.1 mainshock, and dozens of surface breaks, provided a new window into the question. By combining a rich data set of ground shaking and deformation, we found that the ruptures are substantially simpler at depth than near the surface, with four faults explaining all the data reasonably well. Interestingly, both the foreshock and the mainshock started at fault junctions and then ruptured multiple faults. Where the two events overlapped, their slip patterns are largely complementary to each other.

1. Introduction

In July 2019, a sequence of earthquakes including a M_w 6.4 foreshock and a M_w 7.1 mainshock struck the Ridgecrest region in the Eastern California Shear Zone in the United States. This sequence, together with the 1992 M_w 7.3 Landers earthquake and 1999 M_w 7.1 Hector Mine earthquake, account for part of the slip budget between Pacific plate and North America plate (Hauksson et al., 1993, 2002). Field measurements, geodetic observations, and aftershock relocations indicate that the Ridgecrest sequence ruptured the surface along several interlocking and orthogonal faults surrounding the main rupture zone (Ross et al., 2019; Xu et al., 2020). These complexities pose challenges in understanding the rupture physics and regional hazard assessments. Using fault geometry assumptions based on surface traces and aftershock patterns, investigations of the Ridgecrest rupture processes and slip distributions have formed a consensus that the M_w 6.4 foreshock ruptured a NE-SW fault segment, followed by the M_w 7.1 mainshock occurring on the ~40 km NW-SE striking fault (Barnhart et al., 2019; Chen et al., 2020; Goldberg et al., 2020; Liu et al., 2019; Ramos et al., 2020; Ross et al., 2019; K. Wang et al., 2020). However, the kinematic details of the foreshock rupture remain controversial, as some studies suggest the foreshock involved two orthogonal segments (Liu et al., 2019; Ross et al., 2019; Yang et al., 2020), while others prefer that the foreshock only ruptured the NE-SW fault branch(es) (Barnhart et al., 2019; Goldberg et al., 2020). Furthermore, the M_w 7.1 rupture process at depth and its relation with the surface traces are still unclear.

Although surface rupture traces and aftershock distributions are closely related to the fault geometries, faults with major slips at depth may not be directly manifested by these observations. For the Ridgecrest

sequence, the surface trace observations show the multiscale complexity of the fault system (DuRoss et al., 2020; Ponti et al., 2020), which appears inconsistent with the deeper aftershock seismicity (X. Wang & Zhan, 2020a). Specifically, the foreshock surface rupture traces do not verify its NW striking aftershock band, and the mainshock surface ruptures is offset by ~2 km from its aftershock zone at most (Figure 1a). This discrepancy could cause ambiguity in fault geometry choices, thus potentially biasing the slip distribution in finite-fault inversions (Ragon et al., 2019). To characterize the first-order spatiotemporal rupture complexity while avoiding this ambiguity, subevent methods have been developed and successfully applied to complex large earthquakes (Jia et al., 2020; Shi et al., 2018; Zhan et al., 2014). Subevent inversions parameterize earthquakes into multiple point source subevents of varying focal mechanisms, timings, and locations. This parameterization allows simple yet flexible accommodation of multiple fault segments, and often captures the first-order rupture complexities. For example, our previous subevent model of the M_w 6.4 Ridgecrest foreshock shows that it ruptured two conjugate faults (Ross et al., 2019). However, subevent models usually assume point sources and 1-D Green's functions, thus are limited in understanding the relationship between the foreshock and mainshock slip patterns.

3-D seismic structural effects may bias rupture models if not accounted for appropriately (Graves & Wald, 2001). As a good approximation in many cases, 1-D Earth models are broadly used in slip inversions, including most of the studies so far on the Ridgecrest sequence (Chen et al., 2020; Goldberg et al., 2020; Liu et al., 2019; Ross et al., 2019). However, the complex tectonic setting around the Ridgecrest sequence, which sits next to a deep sedimentary basin between the Sierra Nevada and Argus Range, makes it necessary to incorporate a realistic 3-D structural models in the source inversions (X. Wang & Zhan, 2020a). A series of 3-D community velocity models (CVM) for Southern California has been proposed through integrating seismic tomography, reflection/refraction surveys, well logs, and geologic studies (Lee, Chen, Jordan, Maechling, et al., 2014; Small et al., 2017). Examinations of different CVM models suggest that the CVM-S4.26 model well predicts seismograms up to 0.2 Hz (Lee, Chen, & Jordan, 2014). Application of CVM-S4.26 on automated moment tensor inversion in the Los Angeles and Ridgecrest regions also demonstrated the model's effectiveness (X. Wang & Zhan, 2020a, 2020b).

In this paper, we will further improve the subevent inversion with 3-D Green's functions to investigate the rupture processes and fault geometries of the Ridgecrest sequence. We will then use the subevent models to guide multiple-fault slip inversions to reveal details of the rupture processes. While the subevent inversions still use only seismic data, we add geodetic observations to the multifault inversions to provide tighter constraints on the detailed slip patterns. Finally, we will discuss the complexity of the fault system, the relationship between the foreshock and mainshock slips, and the importance of fault junctions in the sequence.

2. Data and Method

We use a variety of data including near-field (within 100 km) strong-motion (0.02–0.2 Hz) and teleseismic (between 30° and 90°) waveforms (0.01–0.2 Hz) (Figure S1 in the supporting information) in subevent inversions, and add near-field high-rate GPS (HRGPS) time series (<0.2 Hz) and interferometric synthetic aperture radar (InSAR) data in our finite-fault analysis. In particular, the dense strong motion data help resolve the rupture episodes, while the teleseismic body waves provide tight constraints on the subevent depths and strike/dip angles, both critical to the accurate determination of fault geometries. For the multifault inversions, we further incorporated the geodetic data including 19 HRGPS stations and InSAR line-of-sight (LOS) measurements from the ALOS-2 and Sentinel-1 satellites. For the HRGPS data used in slip inversions, we excluded the vertical components due to the low signal-to-noise ratio. The InSAR data spans both the M_w 6.4 foreshock and the M_w 7.1 mainshock, providing constraints only on the summation of slip distributions from these two events. Therefore, we forward calculated the LOS displacement of the foreshock slip model derived by other data, subtracted it from the InSAR data, and incorporated the residual displacement field in the mainshock slip inversion together with the other data sets.

For the inversions of the near-field strong-motion and HRGPS data, we used a strain-Green's-tensor based 3-D finite difference (FD) method (Graves, 1996) to compute the 3-D Green's functions (see Text S1 for details). Ray paths for the teleseismic stations are nearly vertical at the source side and therefore less sensitive to lateral structural variations. We applied a propagator matrix method with plane wave approximation (Qian et al., 2017) for generating the teleseismic Green's functions, using a four-layer 1-D model at the source

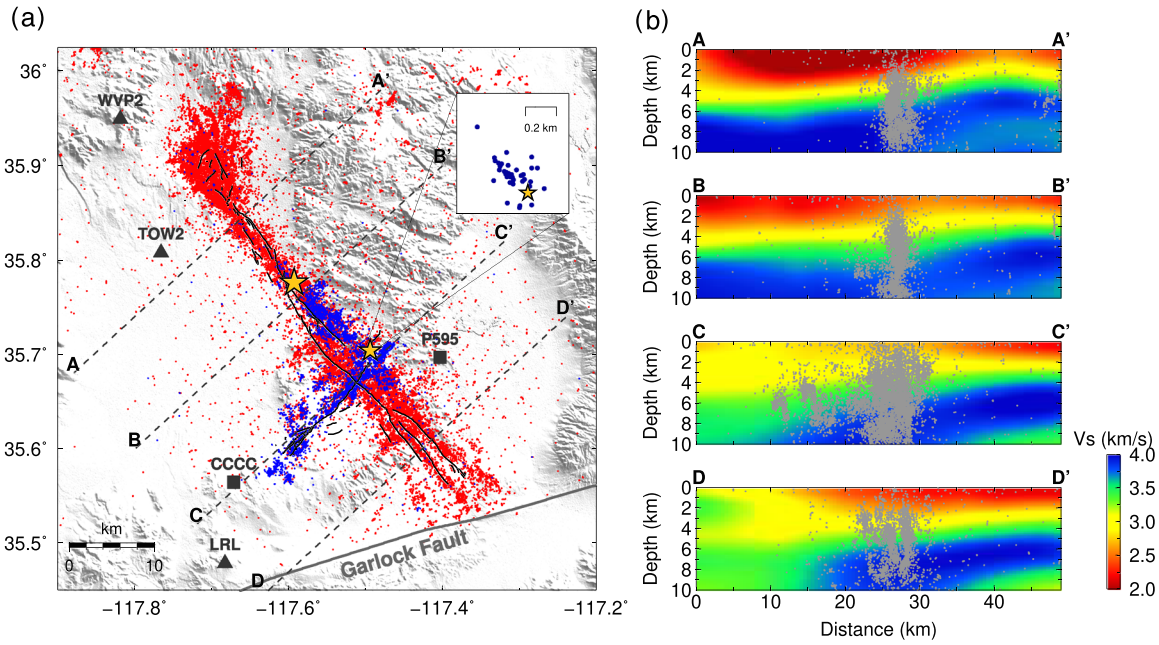

Figure 1. Overview of the seismicity and structure of the Ridgecrest region. (a) Aftershocks and surface ruptures of the Ridgecrest sequence. Events preceding and after the M_w 7.1 mainshock are indicated by blue and red dots, respectively. The inset box shows the foreshocks of the M_w 6.4 event. Black lines delineate mapped surface ruptures (Brandenberg et al., 2019). The black triangles and squares are the seismic and HRGPS stations, respectively. (b) Four cross sections in (a) showing the seismic structure. The background color represents the shear wave velocities from the CVM-S4.26 velocity model (Lee, Chen, Jordan, Maechling, et al., 2014). The gray dots are the Ridgecrest seismicity projected on these planes.

side (Ross et al., 2019). For the InSAR data, we calculated synthetic LOS displacement assuming rectangular subfaults in an elastic half-space (Okada, 1985).

We adopt both subevent and finite-fault inversions to estimate the fault geometries and rupture process. Our subevent method is based on a multiple point source method that was initially performed on deep earthquakes (Zhan et al., 2014; Zhan & Kanamori, 2016), and further developed to accommodate multiple fault ruptures (Jia et al., 2020; Ross et al., 2019). In the subevent inversion, a large earthquake is parameterized by several point source subevents of varying centroid times, durations, locations, and focal mechanisms (Text S2). After we retrieved the subevent model, we determined the number of fault segments and their geometries based on the subevent temporal evolutions, locations, and strike/dip angles. Constraints from subevent centroidal rupture directivity help resolve the nodal plane ambiguities, but choice of the number of faults is still subjective. The subevent models only identify substantially distinct fault geometries while ignoring kinematically insignificant complexities. We grid each fault segment into 2 km * 2 km subfault patches, on each of which the rake angle, rupture time, and rupture speed are determined/guided with the corresponding subevent mechanism, centroid times, and centroidal rupture speed, respectively. We assume the subfault source time function (STF) is a triangle with 2-s duration. With the fault geometry, rake angles, rupture fronts, and shape of STF fixed, the multiple finite-fault problem now reduces to a linearized inversion with slip amplitudes as the only unknown parameters (Hartzell & Heaton, 1983) (Text S3).

3. Results

Figure 2a presents the subevent model and slip distribution of the M_w 6.4 foreshock. With a source duration of ~10 s, the subevent model suggests the foreshock ruptured at least two orthogonal faults. Subevent E1 (M_w 6.1) is located about 3 km northwest of the hypocenter, with a location error of 95% confidence less than 2 km (Figure 2a), suggesting rupture on the northwest striking fault in the first episode. Subevent E2 (M_w 6.1) occurs at the cross of the conjugate faults, followed by subevent E3 (M_w 6.2) located ~10 km southwest, indicating the rupture changes its direction toward the southwest in the second episode. This two-fault

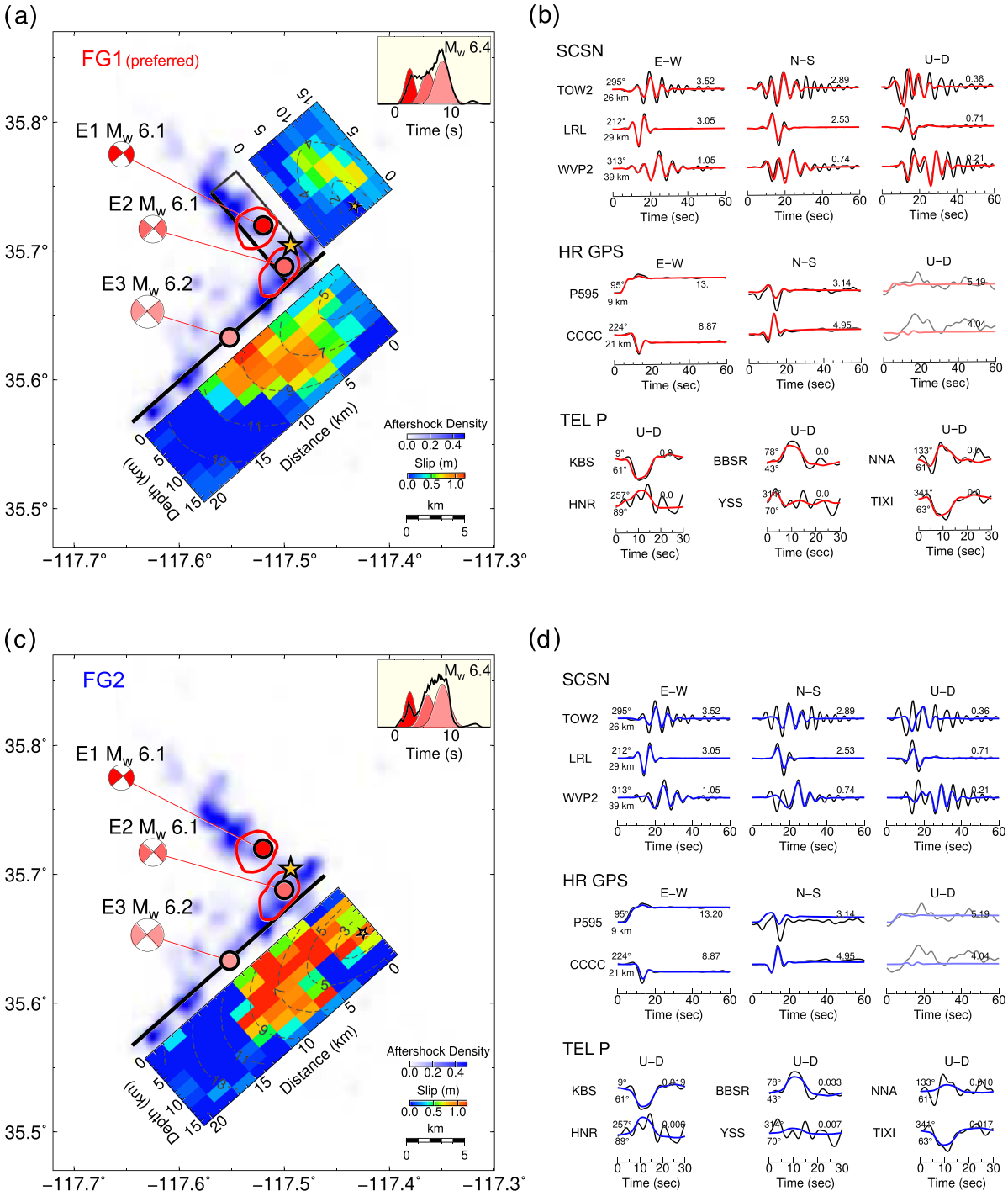

Figure 2. Rupture models of the M_w 6.4 event. (a) Subevent model (red dots and beachballs) and two-fault slip distribution (colored grids). The density of seismicity between the M_w 6.4 and the M_w 7.1 events is displayed by the blue background color. The solid red contours indicate 95% confidential limits of the subevent locations. Subevent E3 is fixed at a location of the maximum surface offset point. The black lines show geometries of the two fault segments: The vertical NE–SW segment is denoted by its surface trace as a thick black line, while the 80° dipping NW-SE branch is projected into a rectangle. The inset box shows moment rate functions of individual subevents (red waveforms), and from the slip model (black line). (b) Representative fits of strong ground motion (SCSN), HRGPS, and teleseismic *P* (TEL P) waves for the two-fault slip model, with data in black and synthetics in red, respectively. The U-D component of HRGPS data, as shown in lighter colors, are not used in the inversion. The numbers leading and tailing the waveforms are the azimuths/distances, and maximum absolute data amplitudes in cm/s (SCSN) or cm (HRGPS and TEL P), respectively. Complete data fittings are shown in Figure S6 in the supporting information. (c) Same as (a) but for the one-fault slip model that only preserves the NE-SW striking segment. (d) Same as (b) but for the one-fault slip mode. The synthetic waveforms are colored in blue.

rupture process agrees with our previous subevent model using 1-D Green's functions (Ross et al., 2019) but has lower uncertainty (Figures S2–S4).

Based on the locations and strike/dip angles of subevents E1 and E3, we constructed two finite-fault planes for slip inversion: NW striking F1 (strike/dip = 320°/80°) and SW-striking F2 (strike/dip = 228°/90°). The centroid times of subevents E1 (2.5 s) and E3 (8.5 s) guided the rupture fronts at the corresponding faults, and the rupture velocity of 2.0 km/s was chosen through a grid search (Figure S5). The depths of rupture onsets on F1 and F2 are 9 and 5 km, the same as the centroid depths of E1 and E3. The slip distribution shows moderate slip (peak slip of 0.7 m) on F1, and major slip (peak slip of 1.2 m) on F2. The F2 slip broke to the surface while the F1 slip did not, consistent with field geology observations (Milliner & Donnellan, 2020). The predicted strong motion, HRGPS, and teleseismic waveforms fit data well (examples in Figure 2b, full data set in Figure S6). We further estimated the uncertainty of our slip model with a cut-half jackknifing approach and found that the slip error is generally less than 10% of the slip values (Figure S7). Due to the limited data resolvability, how the rupture propagated from F1 to F2 through the fault junction remains unclear.

We conducted a test to evaluate the importance of F1, the NW branch of the orthogonal faults, to the M_w 6.4 foreshock data fitting. In addition to our preferred two-fault geometric setting (FG1), we consider an alternative fault geometry (FG2) in which we allow the rupture on the SW-striking F2 only (Figure 2c). The rupture velocity of FG2 is set to be 1.5 km/s to accommodate the rupture beginning on F2. We found that the two-fault model fits the strong motion, HRGPS, and teleseismic waveforms systematically better than the single fault model (Figure 2d). We attribute the improved data fittings, especially for the early wiggles of strong motion waveforms, to the requirement of an initial northwestward rupture directivity. We also tested a third scenario, FG3 (Figure S8) to accommodate a secondary SW-striking surface rupture found in DuRoss et al. (2020). The synthetics for FG3 do not match data as well as the conjugate fault model FG1 (Figure S8), indicating that the first fault ruptured is NW-SE striking.

Our subevent model of the M_w 7.1 mainshock (Figure 3a) shows an initiation with a small subevent E1 (M_w 6.1) close to the hypocenter. As the first episode, the rupture propagated to the northwest indicated by E2 (M_w 6.7) located ~6 km from the hypocenter, then toward the southeast as shown by the largest subevent E3 (M_w 6.8), accounting for over 70% of the total moment. The second episode features a unilateral rupture toward the southwest (subevents E4 and E5). The waveform fittings and uncertainty analysis of the subevent model are shown in Figures S9–S11. Strike angles of all major subevents (E2–E5) are well constrained (Figure S11) to be ~320°, consistent with the throughgoing aftershock band at depth (X. Wang & Zhan, 2020a), but contradicting the curved surface rupture traces (Figure 1a). To reconcile these observations, we set three fault segments for slip inversion, including two major fault segments F1 and F2 and a shallower subparallel fault branch F3 (Figure 3). F1 and F2 have the same strike angle of 320°, and F1 is vertically dipping while F2 has a dip of 80° based on average dip angle of subevents E3–E5. F3 has a strike of 329° following the surface traces, and a dip angle of 70° as guided by the subevent E3's focal mechanism, therefore connects the curved surface traces and the steeper throughgoing faults F1 and F2. Similar to the foreshock inversion, we generated the rupture fronts based on the subevent timings, and attributed an overall rupture velocity of 1.7 km/s based on the timings and locations of subevents E3 and E5. We obtained the best fitting slip model (Figures 3 and S12) with the jackknifing error less than 20% in general (Figure S13). The largest slip asperity occupies the two sides of the hypocenter, corresponding to the subevents E1, E2, and part of E3. Although the throughgoing faults have a maximum slip of ~6 m, the major surface rupture (~4 m) is contributed by the subparallel branch F3, which corresponds to the remainder of E3. The third slip asperity is located at the junction with the orthogonal fault involved in the foreshock, and the fourth further to the southeast, accommodating the subevents E4 and E5. The overall slip distribution along the NW-SE fault agrees with other slip inversions results (Barnhart et al., 2019; Chen et al., 2020; Goldberg et al., 2020).

Though guided by subevent locations and focal mechanisms in our slip inversion, fault geometries are more commonly assumed based on surface traces, centroid moment tensors, or aftershock patterns. To evaluate the different assumptions and their impacts on the models, we generated three alternative fault geometries and compared their slip models with our preferred one (Figure S14). The first fault model FG1, constructed with vertical faults following the surface rupture segments (Goldberg et al., 2020; Pollitz et al., 2020), fails to predict the large teleseismic *P* wave amplitudes from certain azimuths. FG2 is assumed to have a single

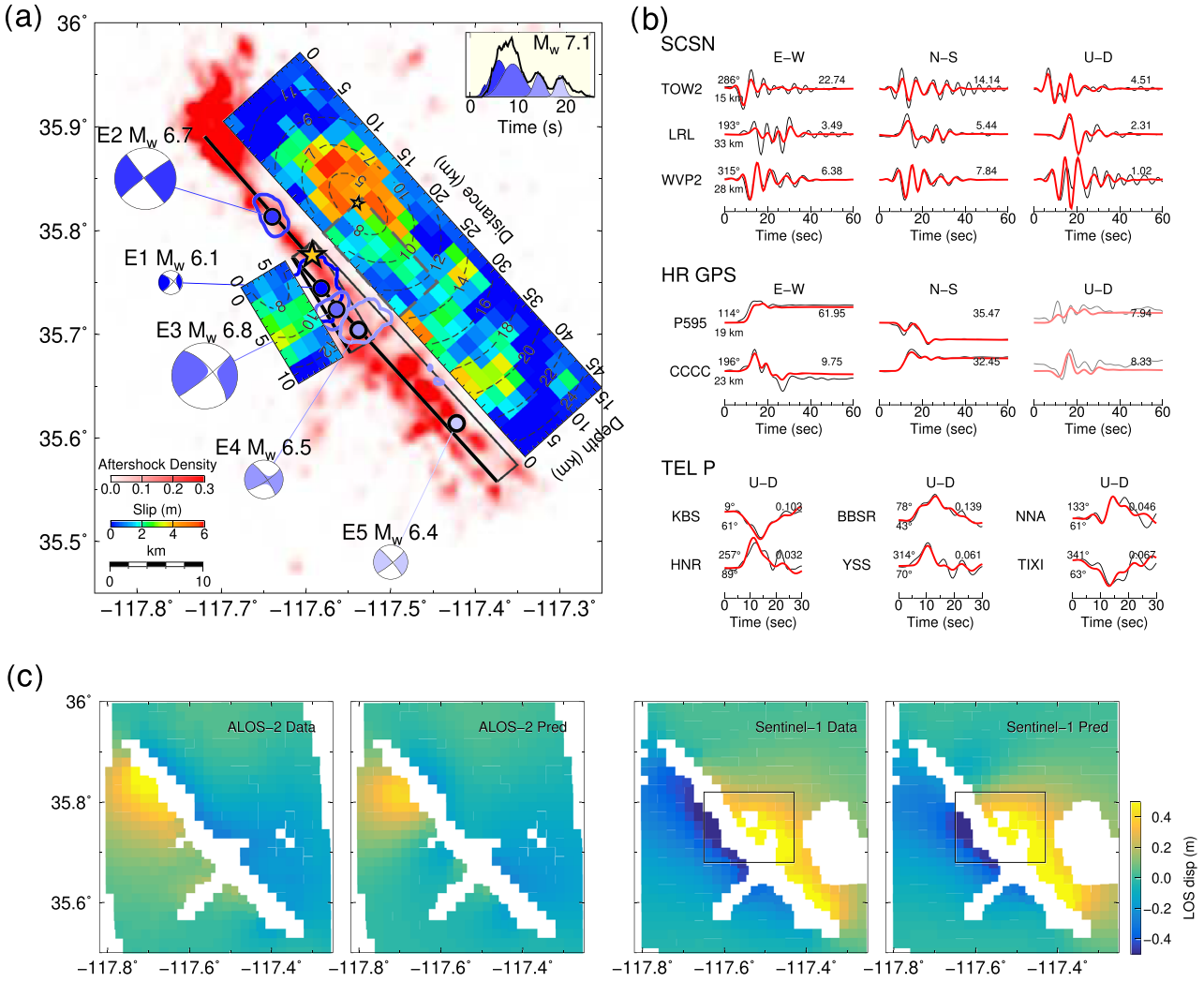

Figure 3. Subevent model and slip distribution of the M_w 7.1 event. (a) Same configuration as Figure 2a, but for the M_w 7.1 mainshock. Aftershocks of the M_w 7.1 event are displayed in red in the background. The blue dots, beachballs, and source time functions indicate the corresponding mainshock subevents. E5 is fixed according to the southeastward slip patch in a static slip model. (b) Same as Figure 2b, but for the mainshock. (c) Decimated data and model predictions for the unwrapped ALOS-2 and Sentinel-1 InSAR line-of-sight displacements. The black box corresponds to the region for model comparison in Figure S14.

vertical fault plane (e.g., Zhang et al., 2020), which is commonly applied when only the centroid moment tensor and/or aftershock distribution is available. This model predicts teleseismic *P* waves slightly better, but is unable to fit the Sentinel-1 InSAR data. Compared with FG2, the southern fault strand of FG3 dips slightly (80°) toward the northeast, and this change produces substantial improvements on the fittings of teleseismic waveforms, yet large misfit for the InSAR data is still observed. FG4, the preferred model in this study as discussed above improves the fitting of Sentinel-1 InSAR data significantly.

4. Discussion

A remarkable feature of the Ridgecrest sequence is the overall lambda-shaped fault configuration with orthogonal segments (Hudnut et al., 2020). Through unconfined subevent inversions and finite-fault modeling with varying fault geometries, we found that the foreshock ruptured two perpendicular fault segments. The rupture on the NW-SE segment is not only supported by the aftershock distributions (Figure 1), but also delineated by a bunch of small earthquakes preceding it (inset box in Figure 1a; Shelly, 2020). The discrepancy between the conjugate aftershocks patterns and the SW striking surface traces can thus be reconciled by the deep slip on the NW striking plane which did not break to the surface (Figure 2a). Coseismic rupture

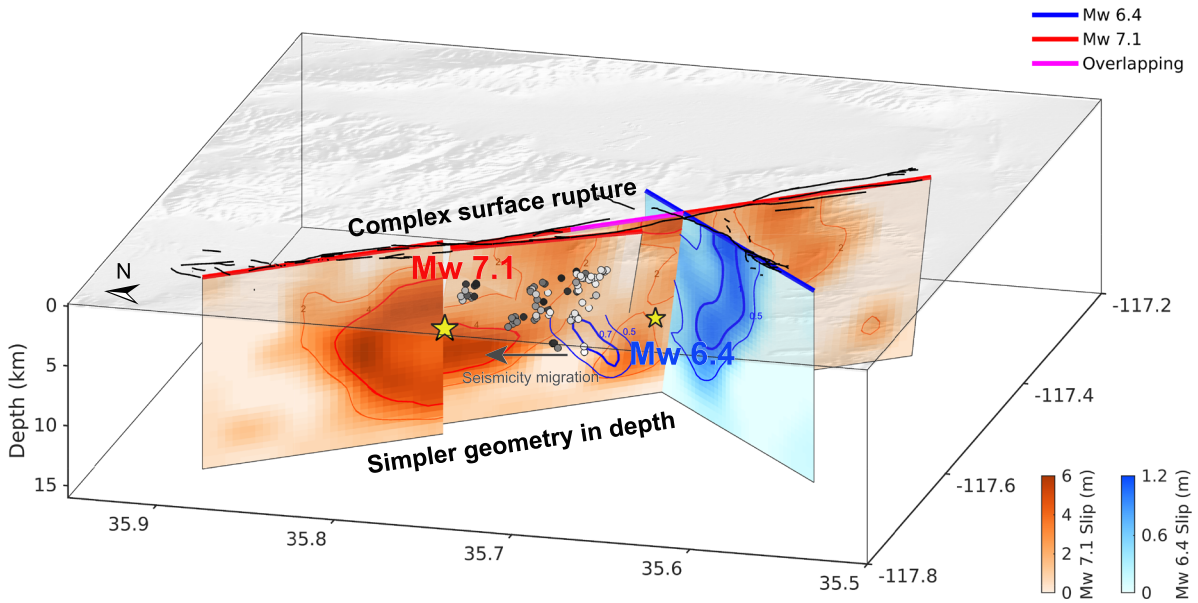

Figure 4. 3-D configuration of the fault system ruptured by the Ridgecrest sequence. Displayed in different color scales, slip contours of the M_w 6.4 foreshock and the M_w 7.1 mainshock are shown in blue and red. Circles of white to black colors indicate the temporal evolution of aftershocks (magnitude > 2.5) between the M_w 6.4 and M_w 7.1 events. Black lines delineate observed surface ruptures. The foreshock ruptures orthogonal fault segments, followed by aftershocks migrating towards the hypocenter of the M_w 7.1 mainshock. The mainshock ruptures subparallel surface traces, but these segments merge to a throughgoing fault in deeper depths.

of orthogonal faults has been considered rare because sharp bends can act as geometrical barriers to earthquakes (Aki, 1979; Nielsen & Knopoff, 1998). But in recent years, orthogonal fault ruptures have been observed for multiple events, including the 2012 Sumatra earthquake (Meng et al., 2012) and the 2018 Alaska earthquake (Lay et al., 2018). This suggests that ruptures can be controlled by the interaction between differently oriented faults, such as weak spots at fault intersections (Talwani, 1999) and transient stress triggering (King et al., 1994). On the other hand, orthogonal fault ruptures could repeatedly occur according to the reported abundance of orthogonal structures in Southern California (Ross et al., 2017), which challenges traditional wisdom of regional hazard assessments.

The M_w 6.4 foreshock and the M_w 7.1 mainshock occurred sequentially within 34 hr in the same fault system, raising the question how these two events associate with each other. Our slip models indicate that the NW-SE striking segment of the foreshock has the same geometric properties as the southern fault segment of the mainshock. Therefore, we suggest it is the same fault ruptured by both events (Figure 4). More specifically, the mainshock ruptured around the high coseismic slip zone of the foreshock at about 10-km depth. The foreshock initiated near the junction of two orthogonal NW and SW striking fault segments, and then ruptured the two sequentially. Although the foreshock northwestward rupture was terminated possibly due to a barrier or the geological complications, it increased the shear stress in the extension of fault. The slip on the orthogonal NE-SW segment can generate positive Coulomb stress change at the mainshock hypocenter as well (Barnhart et al., 2019; Goldberg et al., 2020). These stress perturbations caused the emergence of a number of small events between the foreshock and mainshock in space and time, including a M_w 5.4 earthquake on 5 July. The seismicity slowly migrated toward the northwest (Figure 4) and eventually triggered the nucleation of the M_w 7.1 mainshock at another fault junction. This junction connects a twisted through-going NW-SE striking fault and a subparallel fault segment at shallow depth (Figure 4). Note that the twisting is consistent with the strike variation of surface ruptures (Figure 4), but the deeper aftershocks form a narrow straight band, and the dipping subparallel fault in our model reconciles them, consistent with a systematic study on the source parameters of Ridgecrest aftershocks (X. Wang & Zhan, 2020a). Besides the Ridgecrest foreshock and mainshock, initiation of a multifault earthquake at fault junction has also been observed for the 1999 Hector Mine earthquake (Oglesby et al., 2003), and has been attributed to be potential weak zones due to their geometric incompatibilities (Andrews, 1989; Gabrielov et al., 1996). The instability

of fault junctions has also been associated with enhanced permeability and higher fluid pressure (Sibson, 1996). The mainshock slip distribution complements the foreshock slip on the throughgoing northwest striking fault, suggesting that the mainshock extended the failure and completed the stress release after the foreshock.

5. Conclusion

We developed a novel subevent to multifault approach to estimate the rupture processes and the fault geometries of the Ridgecrest sequence. On 4 July, the M_w 6.4 foreshock initiated near the cross of two orthogonal faults, and ruptured towards NW first and then SW. Although the NW rupture did not extend long, it likely caused dynamic/static stress accumulation at the M_w 7.1 mainshock hypocenter, as manifested by the migration of seismicity. Two days later, the mainshock nucleated at a complex three-fault junction along the extension of the foreshock NW segment. It ruptured first bilaterally, then unilaterally on faults that broke multiple surface traces though merged into a twisted but through-going fault at depth. Its slip distribution complemented the area ruptured by the foreshock. In summary, the Ridgecrest sequence demonstrated remarkable interactions of two multifault ruptures, both started at fault junctions. These observations, which are uncovered by an assembly of seismological, geodetic and remote sensing data sets, attest to the linkage between multi-fault ruptures of the foreshock and the mainshock, as well as the importance of fault junction instabilities.

Data Availability Statement

We thank SCEDC for access to the strong-motion data (https://scedc.caltech.edu), IRIS for the teleseismic waveforms (http://ds.iris.edu/wilber3/find_event), and UNAVCO for the HRGPS observations (https://www.unavco.org/projects/other-projects/high-rate-gps/high-rate-gps.html). We thank the JPL ARIA team for distributing the InSAR data (https://aria-share.jpl.nasa.gov/20190704-0705-Searles_Valley_CA_EQs/SRL-Data_Mine/) (Fielding et al., 2020). We thank SCEC for the Community Velocity Models (https://www.scec.org/research/ucvm).

Acknowledgments
We thank Zachary Ross for the aftershock catalog (https://scedc.caltech.edu/research-tools/QTM-ridgecrest.html), Eric Fielding, Benjamin Idini, Ollie Stephenson for processing InSAR interferograms, and Kejie Chen for processing the HRGPS time series. We thank Kejie Chen, Jean-Philippe Avouac, Joann Stock and Jennifer Jackson for helpful discussions. We thank two anonymous reviewers for suggestions. This work is supported by USGS grant G19AP00030.

References

Aki, K. (1979). Characterization of barriers on an earthquake fault. *Journal of Geophysical Research*, *84*(B11), 6140–6148. https://doi.org/10.1029/JB084iB11p06140

Andrews, D. (1989). Mechanics of fault junctions. *Journal of Geophysical Research*, *94*(B7), 9389–9397. https://doi.org/10.1029/JB094iB07p09389

Barnhart, W. D., Hayes, G. P., & Gold, R. D. (2019). The July 2019 Ridgecrest, California, earthquake sequence: Kinematics of slip and stressing in cross-fault ruptures. *Geophysical Research Letters*, *46*, 11,859–11,867. https://doi.org/10.1029/2019GL084741

Brandenberg, S. J., Wang, P., Nweke, C. C., Hudson, K., Mazzoni, S., Bozorgnia, Y., et al. (2019). Preliminary report on engineering and geological effects of the July 2019 Ridgecrest earthquake sequence, Report of the NSF-Sponsored Geotechnical Extreme Event Reconnaissance Association.

Chen, K., Avouac, J.-P., Aati, S., Milliner, C., Zheng, F., & Shi, C. (2020). Cascading and pulse-like ruptures during the 2019 Ridgecrest earthquakes in the eastern California shear zone. *Nature Communications*, *11*, 22. https://doi.org/10.1038/s41467-019-13750-w

DuRoss, C. B., Gold, R. D., Dawson, T. E., Scharer, K. M., Kendrick, K. J., Akciz, S. O., et al. (2020). Surface displacement distributions for the July 2019 Ridgecrest, California, earthquake ruptures. *Bulletin of the Seismological Society of America*, *110*(4), 1400–1418. https://doi.org/10.1785/0120200058

Fielding, E. J., Liu, Z., Stephenson, O. L., Zhong, M., Liang, C., Moore, A., et al. (2020). Surface deformation related to the 2019 M_w 7.1 and 6.4 Ridgecrest earthquakes in California from GPS, SAR interferometry, and SAR pixel offsets. *Seismological Research Letters*, *91*(4), 2035–2046. https://doi.org/10.1785/0220190302

Gabrielov, A., Keilis-Borok, V., & Jackson, D. D. (1996). Geometric incompatibility in a fault system. *Proceedings of the National Academy of Sciences*, *93*(9), 3838–3842. https://doi.org/10.1073/pnas.93.9.3838

Goldberg, D. E., Melgar, D., Sahakian, V., Thomas, A., Xu, X., Crowell, B., & Geng, J. (2020). Complex rupture of an immature fault zone: A simultaneous kinematic model of the 2019 Ridgecrest, CA earthquakes. *Geophysical Research Letters*, *47*, e2019GL086382. https://doi.org/10.1029/2019GL086382

Graves, R. W. (1996). Simulating seismic wave propagation in 3D elastic media using staggered-grid finite differences. *Bulletin of the Seismological Society of America*, *86*(4), 1091–1106.

Graves, R. W., & Wald, D. J. (2001). Resolution analysis of finite fault source inversion using one-and three-dimensional Green's functions: 1. Strong motions. *Journal of Geophysical Research*, *106*(B5), 8745–8766. https://doi.org/10.1029/2000JB900436

Hartzell, S. H., & Heaton, T. H. (1983). Inversion of strong ground motion and teleseismic waveform data for the fault rupture history of the 1979 Imperial Valley, California, earthquake. *Bulletin of the Seismological Society of America*, *73*(6A), 1553–1583.

Hauksson, E., Jones, L. M., & Hutton, K. (2002). The 1999 M_w 7.1 Hector Mine, California, earthquake sequence: complex conjugate strike-slip faulting. *Bulletin of the Seismological Society of America*, *92*(4), 1154–1170. https://doi.org/10.1785/0120000920

Hauksson, E., Jones, L. M., Hutton, K., & Eberhart-Phillips, D. (1993). The 1992 landers earthquake sequence: Seismological observations. *Journal of Geophysical Research*, *98*(B11), 19,835–19,858. https://doi.org/10.1029/93JB02384

Hudnut, K. W., Brooks, B. A., Scharer, K., Hernandez, J. L., Dawson, T. E., Oskin, M. E., et al. (2020). Airborne lidar and electro-optical imagery along surface ruptures of the 2019 Ridgecrest earthquake sequence, southern California. *Seismological Research Letters*, *91*(4), 2096–2107. https://doi.org/10.1785/0220190338

Jia, Z., Shen, Z., Zhan, Z., Li, C., Peng, Z., & Gurnis, M. (2020). The 2018 Fiji M_w 8.2 and 7.9 deep earthquakes: One doublet in two slabs. *Earth and Planetary Science Letters*, *531*, 115997. https://doi.org/10.1016/j.epsl.2019.115997

King, G. C., Stein, R. S., & Lin, J. (1994). Static stress changes and the triggering of earthquakes. *Bulletin of the Seismological Society of America*, *84*(3), 935–953.

Lay, T., Ye, L., Bai, Y., Cheung, K. F., & Kanamori, H. (2018). The 2018 M_w 7.9 Gulf of Alaska earthquake: Multiple fault rupture in the Pacific plate. *Geophysical Research Letters*, *45*, 9542–9551. https://doi.org/10.1029/2018GL079813

Lee, E. J., Chen, P., & Jordan, T. H. (2014). Testing waveform predictions of 3D velocity models against two recent Los Angeles earthquakes. *Seismological Research Letters*, *85*(6), 1275–1284. https://doi.org/10.1785/0220140093

Lee, E. J., Chen, P., Jordan, T. H., Maechling, P. B., Denolle, M. A., & Beroza, G. C. (2014). Full-3-D tomography for crustal structure in southern California based on the scattering-integral and the adjoint-wavefield methods. *Journal of Geophysical Research: Solid Earth*, *119*, 6421–6451. https://doi.org/10.1002/2014JB011346

Liu, C., Lay, T., Brodsky, E. E., Dascher-Cousineau, K., & Xiong, X. (2019). Coseismic rupture process of the large 2019 Ridgecrest earthquakes from joint inversion of geodetic and seismological observations. *Geophysical Research Letters*, *46*, 11,820–11,829. https://doi.org/10.1029/2019GL084949

Meng, L., Ampuero, J.-P., Stock, J., Duputel, Z., Luo, Y., & Tsai, V. (2012). Earthquake in a maze: Compressional rupture branching during the 2012 mw 8.6 Sumatra earthquake. *Science*, *337*(6095), 724–726. https://doi.org/10.1126/science.1224030

Milliner, C., & Donnellan, A. (2020). Using daily observations from Planet Labs satellite imagery to separate the surface deformation between the 4 July M_w 6.4 Foreshock and 5 July M_w 7.1 mainshock during the 2019 Ridgecrest earthquake sequence. *Seismological Research Letters*, *91*(4), 1986–1997. https://doi.org/10.1785/0220190271

Nielsen, S. B., & Knopoff, L. (1998). The equivalent strength of geometrical barriers to earthquakes. *Journal of Geophysical Research*, *103*(B5), 9953–9965. https://doi.org/10.1029/97JB03293

Oglesby, D. D., Day, S. M., Li, Y.-G., & Vidale, J. E. (2003). The 1999 Hector mine earthquake: The dynamics of a branched fault system. *Bulletin of the Seismological Society of America*, *93*(6), 2459–2476. https://doi.org/10.1785/0120030026

Okada, Y. (1985). Surface deformation due to shear and tensile faults in a half-space. *Bulletin of the Seismological Society of America*, *75*(4), 1135–1154.

Pollitz, F. F., Murray, J. R., Svarc, J. L., Wicks, C., Roeloffs, E., Minson, S. E., et al. (2020). Kinematics of fault slip associated with the 4–6 July 2019 Ridgecrest, California, earthquake sequence. *Bulletin of the Seismological Society of America*, *110*(4), 1688–1700. https://doi.org/10.1785/0120200018

Ponti, D. J., Blair, J. L., Rosa, C. M., Thomas, K., Pickering, A. J., Akciz, S., et al. (2020). Documentation of surface fault rupture and ground-deformation features produced by the 4 and 5 July 2019 M_w 6.4 and M_w 7.1 Ridgecrest earthquake sequence. *Seismological Research Letters*, 1–18. https://doi.org/10.1785/0220190322

Qian, Y., Ni, S., Wei, S., Almeida, R., & Zhang, H. (2017). The effects of core-reflected waves on finite fault inversions with teleseismic body wave data. *Geophysical Journal International*, *211*(2), 936–951. https://doi.org/10.1093/gji/ggx338

Ragon, T., Sladen, A., & Simons, M. (2019). Accounting for uncertain fault geometry in earthquake source inversions–II: Application to the M_w 6.2 Amatrice earthquake, central Italy. *Geophysical Journal International*, *218*(1), 689–707. https://doi.org/10.1093/gji/ggz180

Ramos, M. D., Neo, J. C., Thakur, P., Huang, Y., & Wei, S. (2020). Stress changes on the Garlock fault during and after the 2019 Ridgecrest earthquake sequence. *Bulletin of the Seismological Society of America*, *110*(4), 1752–1764. https://doi.org/10.1785/0120200027

Ross, Z. E., Hauksson, E., & Ben-Zion, Y. (2017). Abundant off-fault seismicity and orthogonal structures in the San Jacinto fault zone. *Science Advances*, *3*, e1601946. https://doi.org/10.1126/sciadv.1601946

Ross, Z. E., Idini, B., Jia, Z., Stephenson, O. L., Zhong, M., Wang, X., et al. (2019). Hierarchical interlocked orthogonal faulting in the 2019 Ridgecrest earthquake sequence. *Science*, *366*(6463), 346–351. https://doi.org/10.1126/science.aaz0109

Shelly, D. R. (2020). A high-resolution seismic catalog for the initial 2019 Ridgecrest earthquake sequence: Foreshocks, aftershocks, and faulting complexity. *Seismological Research Letters*, *91*(4), 1971–1978. https://doi.org/10.1785/0220190309

Shi, Q., Wei, S., & Chen, M. (2018). An MCMC multiple point sources inversion scheme and its application to the 2016 Kumamoto M_w 6.2 earthquake. *Geophysical Journal International*, *215*(2), 737–752. https://doi.org/10.1093/gji/ggy302

Sibson, R. H. (1996). Structural permeability of fluid-driven fault-fracture meshes. *Journal of Structural Geology*, *18*(8), 1031–1042. https://doi.org/10.1016/0191-8141(96)00032-6

Small, P., Gill, D., Maechling, P. J., Taborda, R., Callaghan, S., Jordan, T. H., et al. (2017). The SCEC unified community velocity model software framework. *Seismological Research Letters*, *88*(6), 1539–1552. https://doi.org/10.1785/0220170082

Talwani, P. (1999). Fault geometry and earthquakes in continental interiors. *Tectonophysics*, *305*(1–3), 371–379. https://doi.org/10.1016/S0040-1951(99)00024-4

Wang, K., Dreger, D. S., Tinti, E., Bürgmann, R., & Taira, T. A. (2020). Rupture process of the 2019 Ridgecrest, California M_w 6.4 foreshock and M_w 7.1 earthquake constrained by seismic and geodetic data. *Bulletin of the Seismological Society of America*, *110*(4), 1603–1626. https://doi.org/10.1785/0120200108

Wang, X., & Zhan, Z. (2020a). Seismotectonics and fault geometries of the 2019 Ridgecrest sequence: insight from aftershock moment tensor catalog using 3D Green's functions. *Journal of Geophysical Research: Solid Earth*, *125*, e2020JB019577. https://doi.org/10.1029/2020JB019577

Wang, X., & Zhan, Z. (2020b). Moving from 1-D to 3-D velocity model: Automated waveform-based earthquake moment tensor inversion in the Los Angeles region. *Geophysical Journal International*, *220*(1), 218–234. https://doi.org/10.1093/gji/ggz435

Xu, X., Sandwell, D. T., & Smith-Konter, B. (2020). Coseismic displacements and surface fractures from Sentinel-1 InSAR: 2019 Ridgecrest earthquakes. *Seismological Research Letters*, *91*(4), 1979–1985. https://doi.org/10.1785/0220190275

Yang, J., Zhu, H., & Lumley, D. (2020). Time-lapse imaging of coseismic ruptures for the 2019 Ridgecrest earthquakes using multi-azimuth back-projection with regional seismic data and a 3D crustal velocity model. *Geophysical Research Letters*, *47*, e2020GL087181. https://doi.org/10.1029/2020GL087181

Zhan, Z., & Kanamori, H. (2016). Recurring large deep earthquakes in Hindu Kush driven by a sinking slab. *Geophysical Research Letters*, *43*, 7433–7441. https://doi.org/10.1002/2016GL069603

Zhan, Z., Kanamori, H., Tsai, V. C., Helmberger, D. V., & Wei, S. (2014). Rupture complexity of the 1994 Bolivia and 2013 Sea of Okhotsk deep earthquakes. *Earth and Planetary Science Letters*, *385*, 89–96. https://doi.org/10.1016/j.epsl.2013.10.028

Zhang, Y., Zheng, X., Chen, Q., Liu, X., Huang, X., Yang, Y., et al. (2020). Automatic inversion of rupture processes of the foreshock and mainshock and correlation of the seismicity during the 2019 Ridgecrest earthquake sequence. *Seismological Research Letters*, *91*(3), 1556–1566. https://doi.org/10.1785/0220190343

References From the Supporting Information

Bodin, T., Sambridge, M., Tkalčić, H., Arroucau, P., Gallagher, K., & Rawlinson, N. (2012). Transdimensional inversion of receiver functions and surface wave dispersion. *Journal of Geophysical Research*, *117*, B02301. https://doi.org/10.1029/2011JB008560

Eisner, L., & Clayton, R. W. (2001). A reciprocity method for multiple-source simulations. *Bulletin of the Seismological Society of America*, *91*(3), 553–560. https://doi.org/10.1785/0120000222

Grant, M., & Boyd, S. (2014). CVX: Matlab software for disciplined convex programming, version 2.1, edited.

Hartzell, S. H., & Heaton, T. H. (1986). Rupture history of the 1984 Morgan Hill, California, earthquake from the inversion of strong motion records. *Bulletin of the Seismological Society of America*, *76*(3), 649–674.

Ji, C., Wald, D. J., & Helmberger, D. V. (2002). Source description of the 1999 Hector mine, California, earthquake, part I: Wavelet domain inversion theory and resolution analysis. *Bulletin of the Seismological Society of America*, *92*(4), 1192–1207. https://doi.org/10.1785/0120000916

Jost, M. U., & Herrmann, R. (1989). A student's guide to and review of moment tensors. *Seismological Research Letters*, *60*(2), 37–57. https://doi.org/10.1785/gssrl.60.2.37

Meier, M.-A., Ampuero, J., & Heaton, T. H. (2017). The hidden simplicity of subduction megathrust earthquakes. *Science*, *357*(6357), 1277–1281. https://doi.org/10.1126/science.aan5643

Minson, S. E., & Dreger, D. S. (2008). Stable inversions for complete moment tensors. *Geophysical Journal International*, *174*(2), 585–592. https://doi.org/10.1111/j.1365-246X.2008.03797.x

Zhao, L., Chen, P., & Jordan, T. H. (2006). Strain Green's tensors, reciprocity, and their applications to seismic source and structure studies. *Bulletin of the Seismological Society of America*, *96*(5), 1753–1763. https://doi.org/10.1785/0120050253